Cell

Successful Execution of Working Memory Linked to Synchronized High-Frequency Gamma Oscillations

Jun Yamamoto,[1] Junghyup Suh,[1] Daigo Takeuchi,[1] and Susumu Tonegawa[1,2,*]
[1]RIKEN-MIT Center for Neural Circuit Genetics at the Picower Institute for Learning and Memory, Department of Biology and Department of Brain and Cognitive Sciences, Massachusetts Institute of Technology, Cambridge, MA 02139, USA
[2]Howard Hughes Medical Institute, Massachusetts Institute of Technology, Cambridge, MA 02139, USA
*Correspondence: tonegawa@mit.edu
http://dx.doi.org/10.1016/j.cell.2014.04.009

SUMMARY

Neuronal oscillations have been hypothesized to play an important role in cognition and its ensuing behavior, but evidence that links a specific neuronal oscillation to a discrete cognitive event is largely lacking. We measured neuronal activity in the entorhinal-hippocampal circuit while mice performed a reward-based spatial working memory task. During the memory retention period, a transient burst of high gamma synchronization preceded an animal's correct choice in both prospective planning and retrospective mistake correction, but not an animal's incorrect choice. Optogenetic inhibition of the circuit targeted to the choice point area resulted in a coordinated reduction in both high gamma synchrony and correct execution of a working-memory-guided behavior. These findings suggest that transient high gamma synchrony contributes to the successful execution of spatial working memory. Furthermore, our data are consistent with an association between transient high gamma synchrony and explicit awareness of the working memory content.

INTRODUCTION

Network oscillations are proposed to underlie the temporal binding of spatially distributed neuronal populations to enable information processing for cognition and its ensuing behavior (Singer, 1993). In addition, certain oscillations are hypothesized to allow conscious perception and awareness of associations between external cues and internal goals encoded in the synchronized brain areas (Singer, 1993). In particular, gamma oscillations correlate with perception (Fries et al., 2007; Gray et al., 1989), memory (Fell et al., 2001; Hirabayashi et al., 2013; Jutras et al., 2009; Lisman and Idiart, 1995; Montgomery and Buzsáki, 2007), and attention (Fries et al., 2001). Measuring contingent action selection and neural activity simultaneously in an animal model that allows for neural intervention would enable the relationship between a neural activity, such as gamma oscillations, and a discrete cognitive event to be assessed more precisely.

When rodents engage in a spatial working memory task, two major oscillations of local field potentials (LFP) emerge in both the entorhinal cortex (EC) and hippocampus (HPC) (Bragin et al., 1995). Theta and gamma oscillations represent continuous and transient oscillatory phenomena (Belluscio et al., 2012; Bragin et al., 1995; Chrobak and Buzsáki, 1998; Colgin et al., 2009; Quilichini et al., 2010), respectively. Gamma oscillation frequencies are broad but can be classified as low gamma oscillations (25–50 Hz) and high gamma oscillations (65–140 Hz) (Belluscio et al., 2012; Colgin et al., 2009). Low gamma oscillations typically overlap with the descending phase of the theta oscillation and are hypothesized to be the consequence of CA3 inputs to CA1 (Belluscio et al., 2012). Low gamma oscillations coexist with hippocampal replay events, suggesting that they may coordinate memory reactivation across the hippocampal network during some sharp-wave ripple (SWR) events (Carr et al., 2012). High gamma oscillations are typically phase locked to the trough of the theta oscillation, but their role in the EC-HPC network and in memory, or indeed in any brain circuit or cognitive process, is unknown. We investigated the relationship between synchronized high-frequency gamma oscillations and access to spatial working memory using a delayed nonmatching-to-place (DNMP) T maze task. Our results reveal a tight association of transient cortico-hippocampal high gamma synchrony with the successful use of working memory.

RESULTS

Direct Input from MEC to CA1 Is Crucial for High Gamma Oscillations in CA1 and the Working Memory Task

To block synaptic transmission from the medial EC layer III (MECIII) to CAI, we used triple transgenic mice, ECIII-TeTX mice (see Experimental Procedures for the genotype), in which synaptic transmission from MECIII to CA1 is blocked by tetanus toxin (TeTX) (Figure 1A), resulting in an impairment in spatial working memory (Suh et al., 2011). To detect electrophysiological abnormalities in these mice, which we henceforth refer to as MT (for mutant), we used silicone linear probe arrays to record LFP profiles along the somatodendritic axis of dorsal CA1 (dCA1) of MTs and control littermates (CTs, see

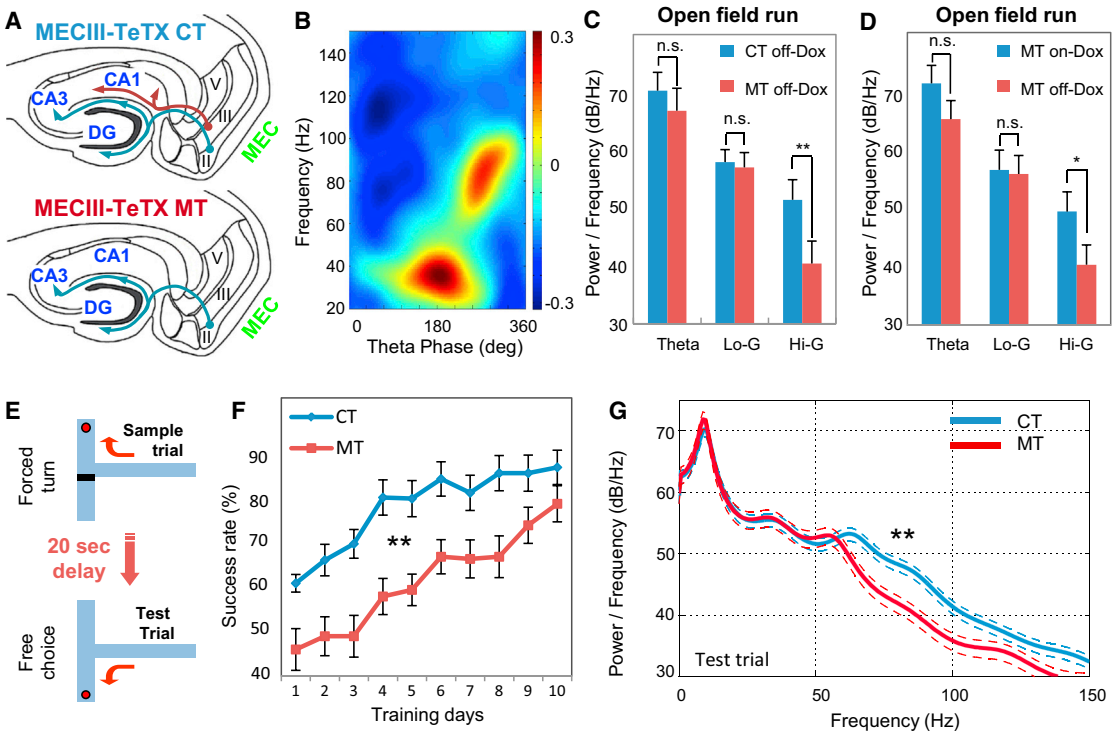

Figure 1. Inhibition of MEC Input to Hippocampal CA1 Impairs Both the Performance and High Gamma Oscillations in Delayed Nonmatch-to-Place Task

(A) Schematic diagram of the major excitatory inputs from MEC to the hippocampus. In both control (MECIII-TeTX CT) and mutant (MECIII-TeTX MT) mice, EC II cells project to the dentate gyrus (DG) and CA3 (blue arrows), but the direct projection of EC III cells to CA1 (red arrows) present in the CT mice is inhibited in the MT mice by transgenic expression of tetanus toxin (TeTX).

(B) Population-averaged plot of cross-frequency coupling of LFP signals in dCA1. LFPs were recorded in dCA1 of MECIII-TeTX CT mice during their exploration in an open field (n = 5 mice). Gamma power was plotted as a function of theta phase. Peak and trough of theta cycle correspond to 90° and 270°, respectively. Color represents the magnitude of power, which was calculated using Morlet's wavelets (see Experimental Procedures).

(C) LFP power in MT and CT during animals' exploration in an open field (n = 5 for each group). Blue, CT; red, MT under off-Dox conditions. Significant difference was found only in the high gamma band (Hi-G). **p < 0.01, paired t test. Error bar represents SD.

(D) LFP power before and after synaptic transmission blockade in MT mice. LFP recordings were first performed under on-Dox conditions and were then performed again 4 weeks after the doxycycline withdrawal (off-Dox) in the same mice while animals were explored in an open field (n = 3 mice). Note the significant reduction in high gamma range, but not in low gamma or theta ranges. *p < 0.05, paired t test. Error bar represents SD.

(E) T maze version of the DNMP task. Sample trial and test trial were separated by 20 s delay. Red dots represent reward, and black bar is a barricade.

(F) Learning curves of MTs and CTs (**p < 0.01, two-way analysis of variance [ANOVA], MT [n = 11] versus CT [n = 12]). Success rate represents the percentage of the correct arm choices during test trials. Error bar represents SD.

(G) Power spectrum density (PSD) estimates for MTs and CTs (7 mice and 210 trials for each) during test trials. Dotted lines, 95% confidence interval. Significant difference was seen only in high gamma band (**p < 0.01, two-sample t test with Bonferroni's correction across LFP sub-bands).

See also Figure S1.

Experimental Procedures for the genotype), and the recorded LFP was categorized into different frequency bands, particularly the two distinct gamma oscillations (Figure 1B and Figure S1A available online). When mice freely explored an open space, high gamma oscillation power, but not theta or low gamma oscillation power, was significantly lower in MTs compared to CTs (Figures 1C, 1D, and S1B–S1E). We also did not detect a significant difference in the frequency, duration, and occurrence of sharp-wave ripples between MTs and CTs (Figure S1F). Autocorrelation analysis showed that the high gamma components were distinct from higher-frequency range oscillations (e.g., >100 Hz), which tend to be susceptible to the possible contamination from spiking activities (Figure S1G). In a delayed nonmatching-to-place (DNMP) T maze task that assays spatial working memory (Figure 1E), MTs showed a significantly delayed learning curve compared to CTs (Figure 1F), as reported previously (Suh et al., 2011). High gamma oscillation power spectral densities (PSDs) were lower during the test trial in MTs compared to CTs, but no effect of TeTX blockade was observed on theta or low gamma oscillation power (Figure 1G).

Pronounced High Gamma Oscillations at T Junction during Test Trials of DNMP Task

We divided the T maze into multiple segments (Figure 2A, 15 cm bins, c1 to c5 for central arm and r1 and r2 for reward arms) and estimated low gamma oscillation and high gamma oscillation power for each segment separately as mice performed the T maze task. We detected transient high gamma and low gamma

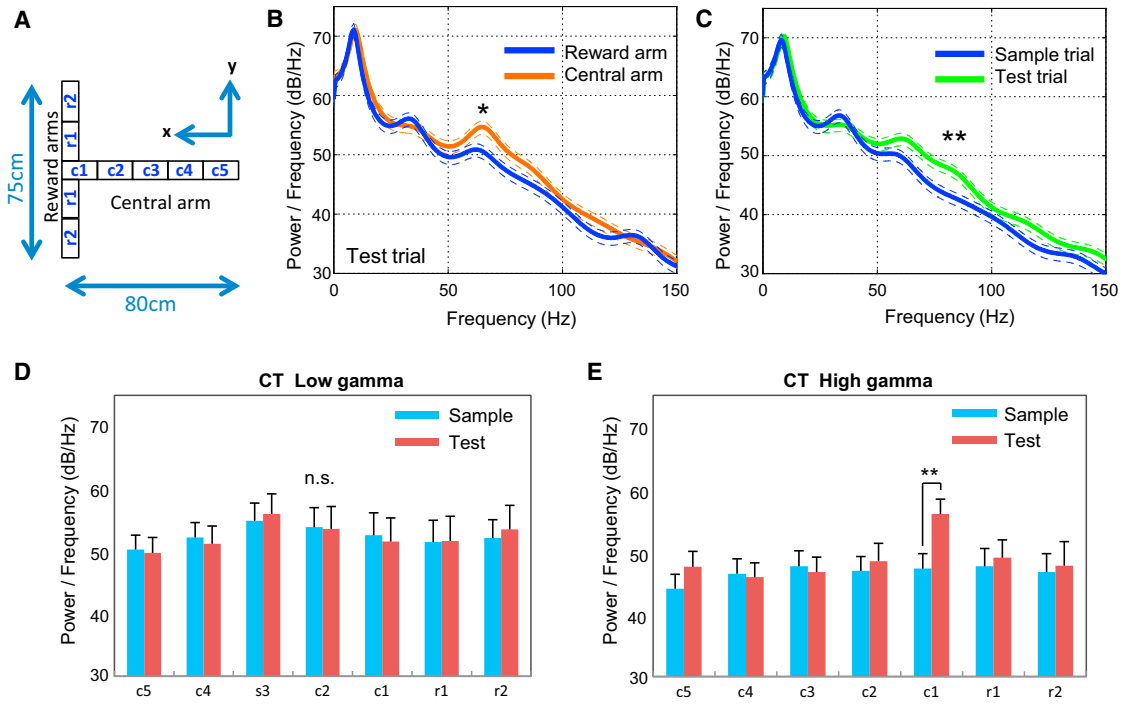

Figure 2. Prominent High Gamma Oscillation Was Observed at the Choice Point during a Test Trial

(A) T maze was divided into multiple segments (c1-5 for central arm and r1-2 for reward arms). Spatial bin size, 15 cm.

(B) CTs displayed greater high gamma power in central arm than reward arms during test trials (**$p < 0.05$, two-sample t test with Bonferroni's correction across LFP sub-bands, 7 mice, 210 sessions). Dotted lines indicate 95% confidence interval.

(C) Greater high gamma power during test trials than sample trials in CT (**$p < 0.01$). Dotted lines, 95% confidence interval.

(D) Power in low gamma band during sample and test trials for each T maze segments. No significant difference was observed across segments and between sample and test trials (two-way ANOVA, CT [n = 7], 280 trials). Error bar represents SD.

(E) Same format as in (D) but for high gamma band. The greatest power was detected in the c1 segment during test trials (*$p < 0.01$, two-way ANOVA followed by the least significant difference [LSD]). Error bar represents SD.

See also Figure S2.

incidents (HGIs and LGIs, respectively) by thresholding the power at the 3 SD of the baseline level (see Experimental Procedures for details). HGIs were predominantly detected just before the animals reached the T junction (Figure S2A). Population analysis showed that the power of HGIs, but not the power of LGIs, was greater in the central arm compared to the reward arms in test trials (Figure 2B) and greater in test trials than in sample trials (Figure 2C). The power of HGIs was significantly greater in the segment closest to the T junction (i.e., c1) compared to other segments during test trials (Figures 2D and 2E). The enhanced high gamma oscillation power during test trials tended to dissipate as the animals became overtrained and presumably employed a different strategy to resolve the T maze task (i.e., more than 18 days of training, Figures S2B and S2C).

High Gamma Oscillation Phase Synchrony between MEC and CA1 during Successful DNMP Trials

We performed dual-site LFP recordings from dCA1 and dorsal MEC (dMEC) superficial layers of wild-type mice. An oscillatory phase synchrony analysis (Figures 3A and S3) (Lachaux et al., 1999; Rodriguez et al., 1999) revealed that HGIs in dCA1 and dMEC became phase synchronized (for the phase relationship between dCA1 and dMEC, see Figure S3A) when the mouse approached the T junction in test trials and made a correct arm choice (Figures 3B and S3B) (for the detection criteria of synchronized high gamma incidents [sHGIs], see Experimental Procedures). No enhanced synchronization of HGIs was observed during sample trials (Figure 3C as an example) or test trials in which the mouse made an incorrect choice (Figure 3D as an example). LGIs were generally infrequent in MEC, and no major synchrony was observed (Figures 3B–3D, S3B, and S3C as examples). Figures 3E and 3F show quantitative comparisons of cumulative sHGIs during test versus sample trials and success versus failure test trials, respectively, as a function of the track segments in which the animals were located. We found that the phase synchrony started to diverge between sample and test trials in c3, and the difference reached a statistically significant level in c1 (Figure 3E). We also found that the phase synchrony started to diverge between success and failure trials in c2, and the difference reached a statistically significant level in c1 (Figure 3F). Similar results were obtained when we used smaller or larger segmentations of the T maze (Figure S3D) or used different passband settings (Figure S3E). We further determined the distributions of sHGI candidates and significant sHGI events (see Experimental Procedures) found during

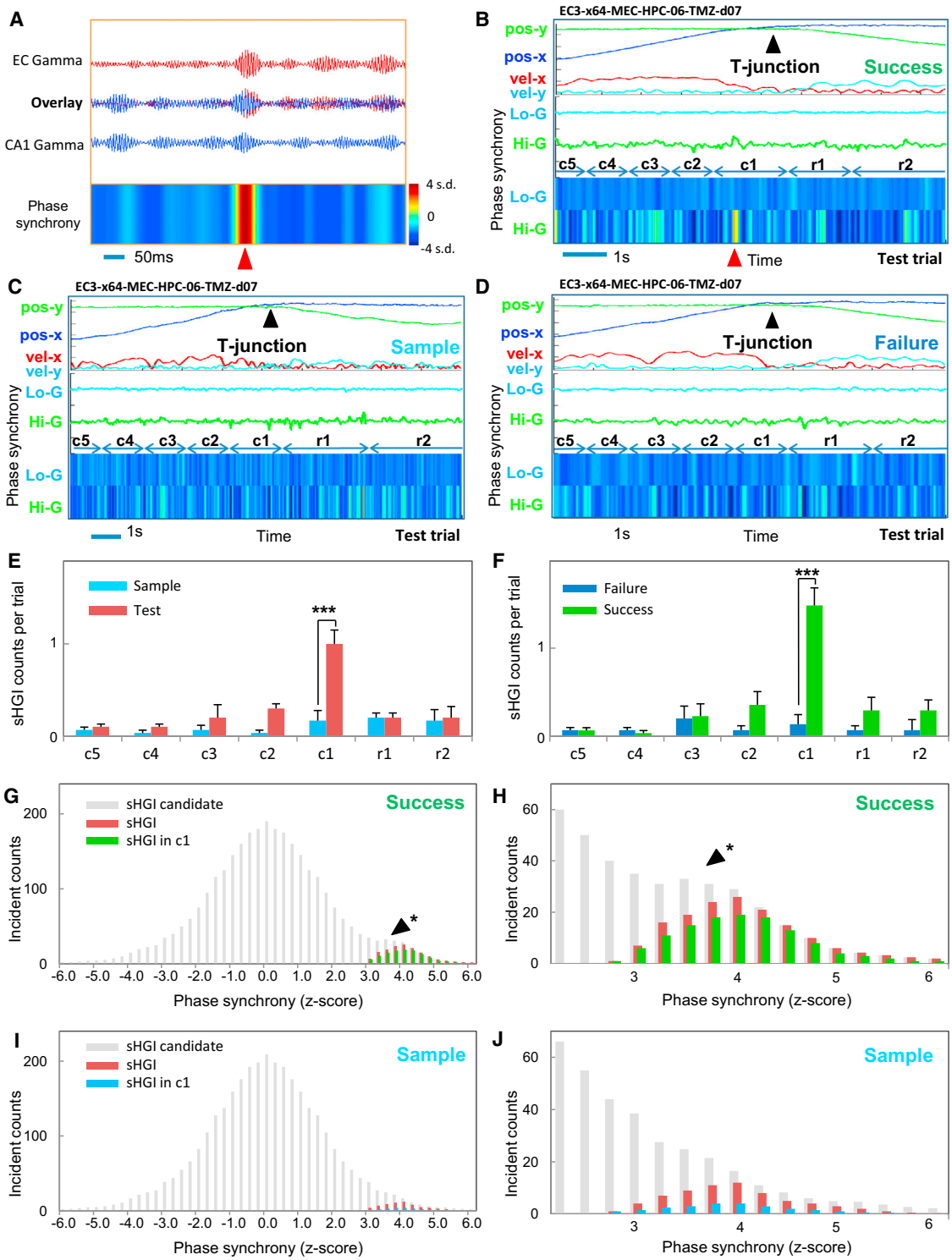

Figure 3. High Gamma Phase Synchrony between MEC and dCA1 at the T Junction of Successful Test Trials

(A) An example of high gamma phase synchrony between the MEC and dCA1. (Top) High gamma oscillation traces of MEC (red) and dCA1 (blue) and their overlay. (Bottom) A heatmap of phase synchrony. Red arrowhead indicates an HGI with the statistically significant synchrony. Color coding represents relative phase synchrony scaled between −4SD and 4 SD. Basic characteristics of synchronized HGI: the duration, 72 ± 22 ms (mean ± SD); the power of high gamma oscillation during sHGI, 46 ± 7 μV and 148 ± 10 μV for MEC and CA1, respectively.

(legend continued on next page)

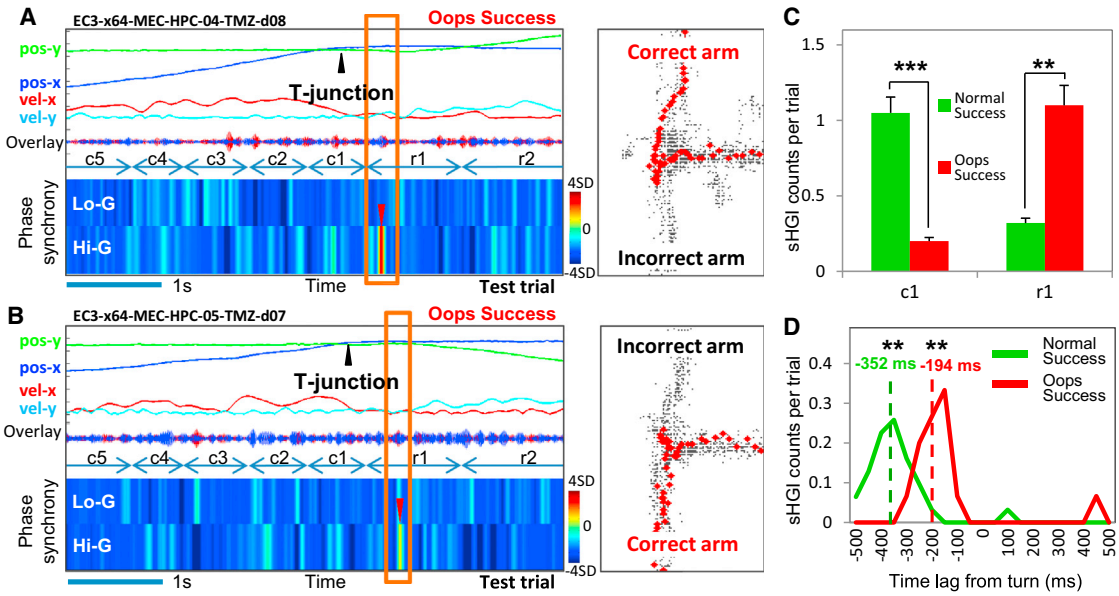

Figure 4. Synchronized High Gamma Incidents Shift in Self-Correction Trials

(A) An example of an sHGI (red arrow) shifted to the r1 segment of the incorrect reward arm during an oops success trial. "Overlay" indicates an overlay of MEC high gamma and dCA1 high gamma oscillations. (Right) The actual trace of animal's positions (red dots) during this particular trial and animal's cumulative positions (black dots) during the entire ten test trials session.

(B) Another example of the oops case but toward the direction opposite to the example in (A).

(C) The number of sHGIs per trial in c1 and r1 segments compared between normal success trials and oops success trials (***$p < 0.001$, **$p < 0.01$, two-sample t test, 5 mice, 162 cases and 21 cases for normal success and oops success, respectively). Error bar represents SEM.

(D) Distributions of time lag of sHGIs from T junction for normal success and oops success trials (**$p < 0.01$, binominal test, median −352 ms from normal success trials and −194 ms from oops success trials).

See also Figure S4 and Movie S1.

success test trials and sample trials as a function of the magnitude of phase synchrony (Figures 3G–3J). As is consistent with the Figures 3E and 3F results, much greater numbers of sHGIs were detected in success trials than in sample trials, and the majority of these incidents in success trials occurred in the c1 segment (Figures 3H and 3J).

Synchronized High Gamma Incidents Dynamically Shift in Time and Space during Self-Correcting Behavior

In some test trials (21 trials out of a total of 200 trials monitored) of all wild-type (5 out of 5) that were in earlier stages of training (days 5 to 9), some animals momentarily entered the wrong arm but quickly corrected their choice by changing their heading within the r1 segment and completed the trial successfully (dubbed "oops" case) (Figures 4A, 4B, S3C, S4A, S4C, and Movie S1). In these cases, the sHGIs with the highest synchrony shifted from a point in c1 to the point where the mice were about to make the directional change in r1 (Figures 4A, 4B, S3C, S4A and S4C). The shift in the location of sHGIs with the highest synchrony from segment c1 to r1 was significant between normal success trials and oops success trials (Figure 4C). The shifted sHGIs on oops success trials occurred at around

(B) An example phase synchrony spectrum of a success test trial with synchronized HGI in c1 (red arrowhead). Animal identity (ID) with recording day ID is on the top of the panel. Lo-G, low gamma; Hi-G, high gamma; pos-x, x position; vel-x, velocity in x position; vel-y, velocity in y position.

(C) An example phase synchrony spectrum of a sample trial. Note no synchronized HGI throughout the trial. Same animal ID and recording day ID as in (B).

(D) An example phase synchrony spectrum of a failure trial with no synchronized HGI throughout the trial. Same animal ID and recording day ID as in (B).

(E) Spatial distribution of sHGI counts on the T maze during sample and test trials. Synchronized HGIs mostly occurred in c1 of test trials (***$p < 0.001$, two-way ANOVA followed by LSD, 5 mice, 150 trials). Error bar represents SEM.

(F) Spatial distribution of sHGI counts on the T maze during success and failure test trials. sHGI mostly occurred in c1 of success test trial (***$p < 0.001$, two-way ANOVA followed by LSD, 5 mice). Error bar represents SEM.

(G) Distribution of sHGI candidates, sHGIs, and sHGIs at c1 in success test trials as a function of phase synchrony (z score). Gray, sHGI candidates. Note that the distribution of sHGI candidate is bimodal (*$p < 0.05$, Hartigan's Dip test). Red, sHGIs; green, sHGIs detected at c1 segment of the maze. An sHGI candidate is "a high gamma incident" in which high gamma power exceeded the 3 SD level of the baseline either in dCA1 or in MEC (see Experimental Procedures for details).

(H) An expansion of the portion of (G) where phase synchrony is higher. *$p < 0.05$, Hartigan's Dip test.

(I) Same as in (G) but for sample trials. Gray, sHGI candidates. Note that the distribution of sHGI candidate is unimodal (n.s., $p = 0.44$, Hartigan's Dip test). Red, sHGIs; blue, sHGIs detected at c1 segment of the maze.

(J) An expansion of the portion of (I) where phase synchrony is higher (n.s., $p = 0.44$, Hartigan's Dip test).

See also Figure S3.

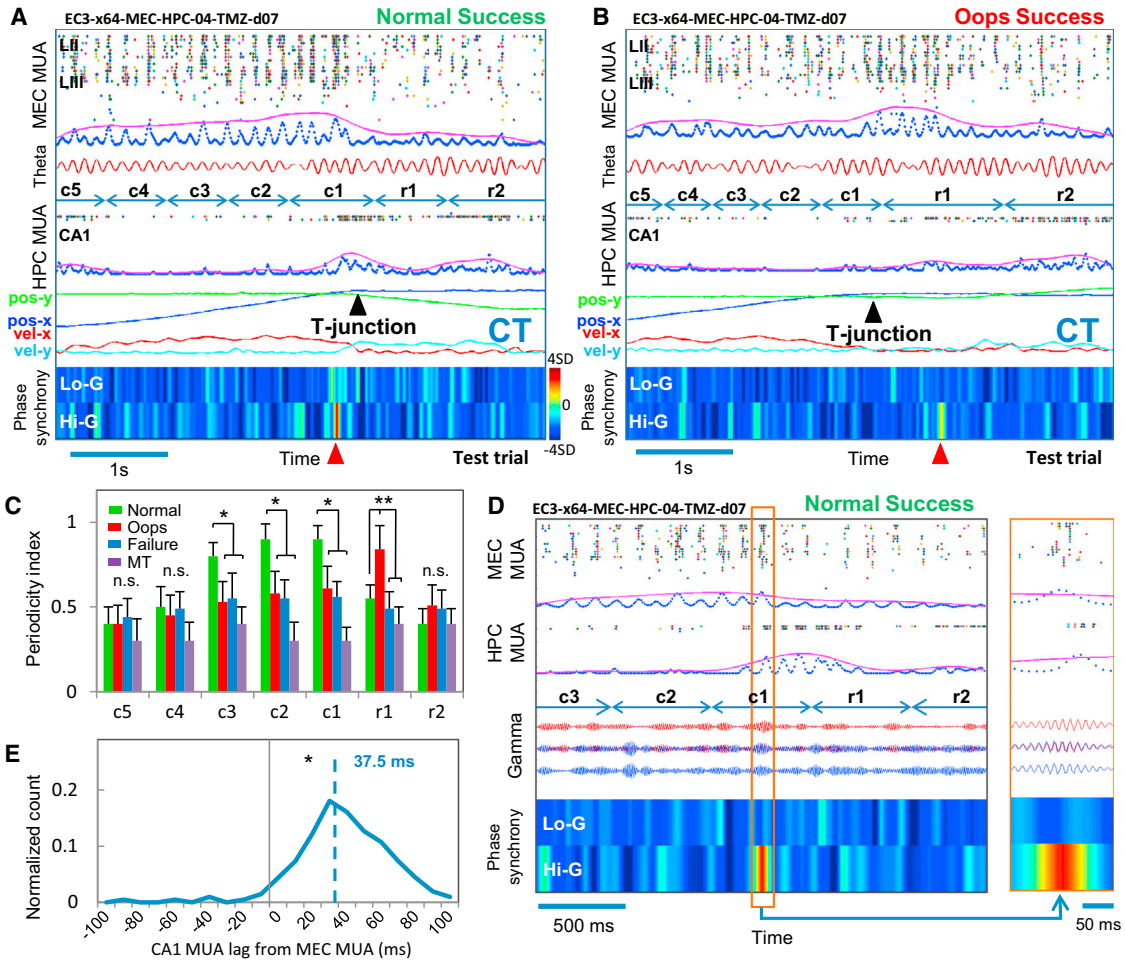

Figure 5. Synchronized High Gamma Incidents and Multiunit Activity Bursts

(A) An example of CT's multiunit activity (MUA) from dMEC and dCA1 during a normal success test trial. (Top) MUA raster recorded from superficial dMEC. Each spiking event is randomly assigned to seven different colors to enhance the visualization of individual events. Blue and magenta lines, smoothed MUA traces (Gaussian kernels, $\sigma = 20$ ms and 80 ms, respectively). Red trace, theta LFP power. (Middle) Same as above but from dCA1. (Bottom) Phase synchrony spectrums in low gamma (Lo-G) and high gamma (Hi-G) bands. Red arrowhead indicates an sHGI.

(B) Same as in (A) but from an oops success test trial of CT.

(C) Periodicity index (see Experimental Procedures) of MUA in dMEC. Strong periodic bursts were observed at c1–c3 during normal success test trials of CT (**$p < 0.01$, *$p < 0.05$, two-sample t test with Bonferroni's correction, 5 mice, 150 trials). There were no significant differences in the periodic bursts among multiple segments during failure test trials of CTs nor among multiple segments during all test trials of MTs. Error bar represents SEM.

(D) An example showing the temporal relationship of MUA between dMEC and dCA1 during an sHGI.

(E) Temporal lag of MUAs in dCA1 relative to those in dMEC. For each sHGI, the centers of mass of the timestamps of MUAs were calculated for dCA1 and MEC, and then the temporal lag between them was calculated (also see the right panel in Figure 4D for an example MUAs during an sHGI). A distribution of the temporal lags for all sHGIs was plotted (n = 3,240 sHGIs in total; *$p < 0.05$, one-sample t test; median, 37.5 ms).

See also Figure S5.

200 ms prior to the directional reversal, whereas during normal success trials, the highest sHGIs occurred at around 350 ms before mice made the turn (Figure 4D). Behaviorally, there was not a significant difference in the animal's trajectories along the central arm between right-turn and left-turn trials (Figure S4D).

Ramping Phasic Multiunit Activity Bursts in MEC during Test Trials of the DNMP Task

We next analyzed the spiking activity in dMEC and dCA1 as animals performed the DNMP task. In CTs, we found strong periodic bursts of multiunit activity (MUA) in dMEC that were phase locked to the local theta oscillation (Figure S5A) as they traversed the central arm during success test trials (examples in Figures 5A and S5B). These MUA bursts were sparse in c5 and c4, ramped up toward the T junction in c3 to c1, and rapidly returned to sparse levels in r1 and r2. In failure test trials, however, the MUA bursts did not ramp up (Figure S5D). In oops success trials, MUA bursts and their periodicity remained low in the central arm, elevated to higher levels in the following r1 segment, and subsided as the mice entered

r2 (Figure 5B). During sample trials, MUA bursts in dMEC gradually increased toward the T junction but remained high in r1 and r2 (an example in Figure S5C). MUA bursts in dMEC remained sparse throughout the test trials in MTs (an example in Figure S5E). A population analysis confirmed a significant increase in dMEC MUA bursts and their periodicity as CTs traversed the central arm toward the T junction during success test trials (Figure 5C), as well as sustained MUA bursts after the T junction during CT sample trials (Figure S5F). Interestingly, in failure trials, MUA bursts and their periodicity remained relatively low in dMEC throughout the test trials (Figures 5C and S5D). MUA bursts in MTs were much weaker in dMEC compared to CTs, and no obvious ramping was observed toward the T junction (Figure 5C). In dCA1 of CTs, MUA bursts were relatively sparse during test trials compared to dMEC. Nevertheless, a closer analysis of the data revealed heightened burst activities in dCA1 during sHGIs associated with the T junction, which were delayed by about 38 ms compared to dMEC (an example: Figure 5D; group data: Figure 5E). In contrast, we did not detect any sustained bursts in dCA1 of MTs, and MT firing rates were relatively high throughout the trials. To examine whether the high gamma oscillations are linked to spiking output, we also analyzed the phase locking of MUAs in dCA1 to LFP and found that MUAs were phased locked to the high gamma oscillations (Figure S5H). These ramping phasic MUA bursts in MEC during success test trials and delayed ramping during oops success trials are followed by sHGIs and may be a key for successful working memory.

Targeted Inhibition of Direct Inputs from MEC to CA1 Reduces Synchronized High Gamma Incidents and Impairs DNMP Performance

Finally, we applied an optogenetic intervention to MEC-specific Cre transgenic mice, pOxr1-Cre, that had been infected bilaterally with the Cre-dependent AAVrh8-DIO-eArchT-eYFP virus (MECIII Cre-eArchT mice) (Figures 6A and 6B). Figure 6C shows that green light (561 nm, 20 mW) suppressed action potentials in dCA1 of anesthetized MECIII Cre-eArchT mice (for the negative control data with blue light [473 nm], see Figure S6A). Bilateral implantation of hybrid fiberopto-silicone linear probe arrays into the HPC (Figure 6B) and illumination of green light (561 nm, 20 mW) to ECIII cell axonal terminals in dCA1 allowed us to inhibit MECIII input into the HPC while keeping MEC activity intact (Kitamura et al., 2014) (Figure S6B). High gamma oscillations but neither theta nor low gamma oscillations were inhibited when light illuminated the HPC while animals were exploring freely in open space (Figures 6D and 6E). Following a 5–9 day training period on the T maze task, mice were subjected to optogenetic manipulations. When green light was delivered to dCA1 while the mice were in c1-c3 during test trials, the average DNMP success rate was reduced by 50% (Figure 6F middle). We further investigated the effect of light illumination on synchronized high gamma incidents. sHGIs are a composite measure of the phase synchrony and power of high gamma oscillations (see Experimental Procedures). Because an inhibition of MEC input to CA1 reduces the power of CA1 high gamma oscillations (Figure 1D), the optogenetic inhibition procedure could reduce sHGIs through this effect on this power. To avoid this possibility, we determined pure synchronized high gamma incidents (psHGIs) (see Experimental Procedures). Illumination of green light during c1-c3 of test trials (most sHGIs occur in the c1-c2 segments of test trials, Figures 2G–2J) reduced the average psHGIs counts by 20% (Figure 6G). In contrast, there was no effect on the success rate (Figure 6F) nor on the psHGI count (Figure 6G) when illumination was restricted to periods during which the mice were in c1-c3 during sample trials (Figure 6F, left) or c3-c5 during test trials (Figure 6F, right). A significant coordinated reduction in the success rates and psHGI counts in c1 of test trials was observed among individual mice that received light during test c1-c3, but not in mice that received light during sample c1-c3 or test c3-c5 (Figure 6H). In addition, theta-locked MUA bursts were significantly reduced in c1 and c2 segments when light was delivered during test c1-c3 (Figure 6I). This is consistent with the previously mentioned ramping MUA in MEC (Figure 5C) that is followed by sHGIs, which highly correlates with the animal's memory performance.

DISCUSSION

Our main finding in this study is that high-frequency gamma synchrony (sHGIs) between the dorsal part of HPC CA1 and the superficial layers of the MEC is associated with the successful execution of spatial working memory (Figures 3B and 3F). This was demonstrated by the pronounced occurrence of sHGIs specifically at the T junction of success test trials in a DNMP T maze task, but not in failure test trials (Figures 3D and 3F). The tightness of this association was supported by our findings in oops success trials, in which the animals momentarily entered the wrong arm but quickly corrected their behavior by reversing their run direction. In these cases, sHGIs shifted in time and space to the point just prior to the directional change (Figures 4A, 4B, S3C, S4A and S4C). This dynamic shift of sHGIs suggests that they contribute to the subject's active recall of the spatial working memory for the correct arm choice (Figure 4C). The observation that optogenetic inhibition of MECIII input to CA1 targeted to the restricted area, including the T junction in test trials, resulted in coordinated reductions of high gamma synchrony at the T junction (Figure 6G), and the rate of successful performance (Figure 6F) is consistent with the relationship of the former with the latter (Figure 6H), though reduced dCA1 spiking due to the intervention may have also contributed to the observed behavioral deficit. Moreover, the observation that high gamma synchrony incidents preceded both arm choices in normal success trials (Figure 3B) and arm correction in oops trials (Figures 4A, 4B, S3C, S4A and S4C) is consistent with the notion that synchronized high gamma oscillations contribute to the animals' correct arm choice rather than being a consequence of their choice.

MEC-CA1-MEC Loop as the Potential Storage Site for Intratrial Working Memory

Working memory during DNMP consists of two parts: rule memory and intratrial memory. Rule memory is thought to be encoded in prefrontal/orbitofrontal neurons (Otto and

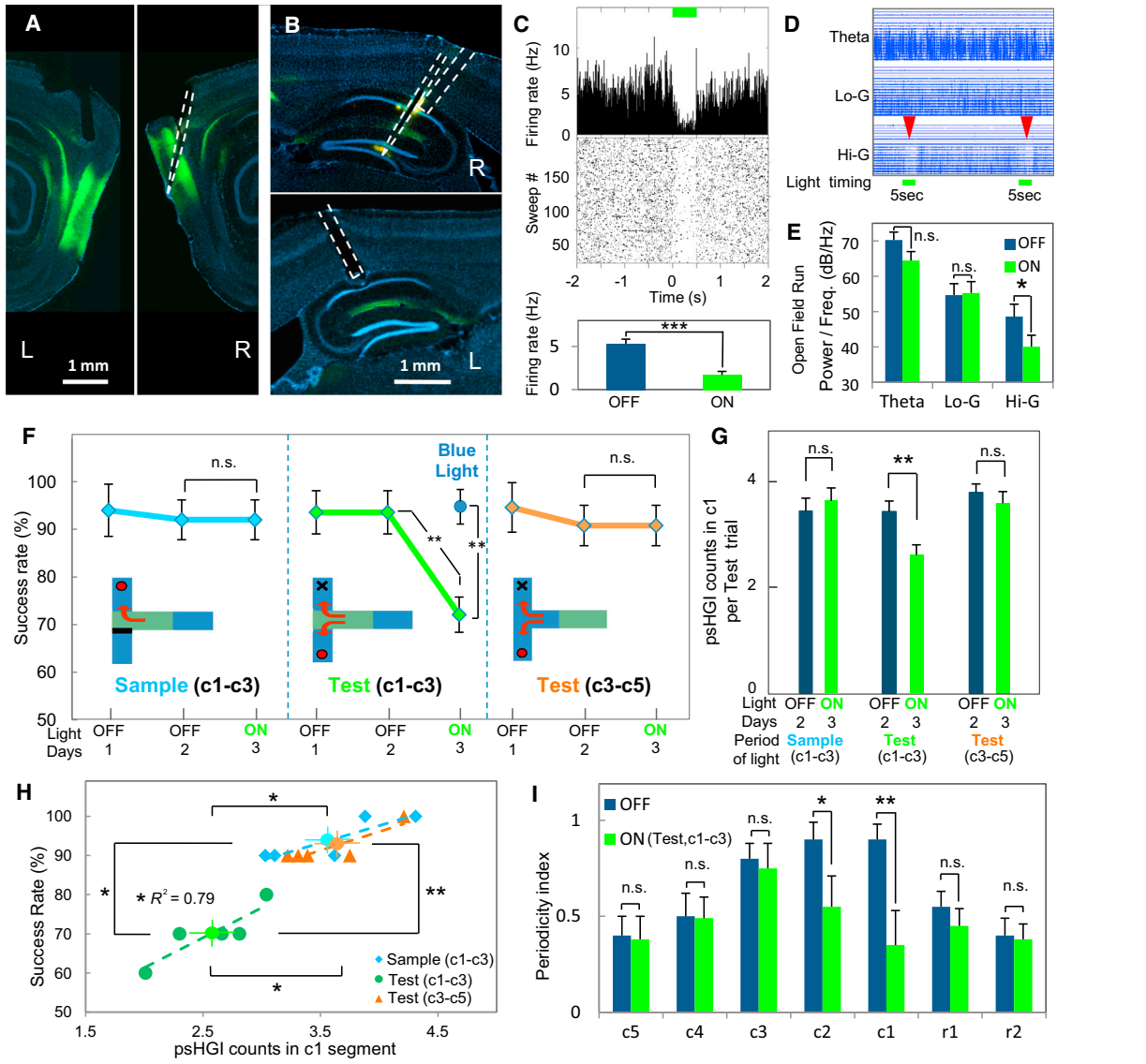

Figure 6. Optogenetic Intervention of Synchronized High Gamma Incidents and Memory Performance

(A) Sagittal sections of MEC regions in the left (L) and right (R) hemispheres of the brain of an MECIII-specific Cre mouse after bilateral injection of AAVrh8-DIO-eArchT-eYFP virus into the MECIII regions. The mouse had implantations of an electrode targeted to the MEC of the right hemisphere. An optical fiber was also targeted to the area just above the pyramidal cell layer of the dCA1 region of the left hemisphere, and a combined electrode-optical fiber was targeted to dCA1 of the right hemisphere. The green fluorescence demonstrates expression of eArchT-eYFP in the MECIII pyramidal cells, and the white dashed lines delineate the electrode track. The sections were counterstained with a nuclear marker DAPI (blue).

(B) Sagittal sections containing the right (R) and left (L) hippocampi of the same mouse as the one used in (A). eArchT-eYFP (green) was observed in the stratum lacunosum-moleculare areas of dCA1 as a consequence of axonal projections of MECIII pyramidal cells. White dashed lines delineate tracks of electrode coupled with optical fiber (top) and the track of optical fiber (bottom). DiI (orange in top panel) was applied to the electrode to help to identify the electrode track. Brain sections were counterstained by DAPI (blue).

(C) (Top) An example of light-induced inhibition of dCA1 MUA in an anesthetized pOxr1-Cre/eArchT-eYFP mouse (561 nm, green horizontal bar at the top). (Bottom) Averaged data of the firing rate in dCA1 during light-on and light-off periods (n = 3 mice, ***p < 0.001, paired t test). Error bar represents SD.

(D) An example of light effects on LFPs in dCA1 in a freely moving animal. The light illumination (green bars) reduced high gamma (Hi-G, red arrows), but not low gamma (Lo-G) or theta.

(E) Averaged population results of light effects on LFPs in dCA1. Significant decrease in power spectral density was observed only in high gamma (Hi-G) during the light illumination (*p < 0.05, paired t test, n = 5). Error bar represents SD.

(F) Optogenetic manipulation during DNMP task. Light was delivered, shown in green, during c1-c3 of sample trials (left), c1-c3 of test trials (middle), and c3-c5 of test trials (right). Control condition with blue light (20 mW, n = 5) on day 4 shown in the middle panel. Five mice for each group. Task performance decreased only when light was delivered during c1-c3 in test trials (**p < 0.01, paired t test). Error bar represents SD. See Experimental Procedures for more detailed procedures.

(legend continued on next page)

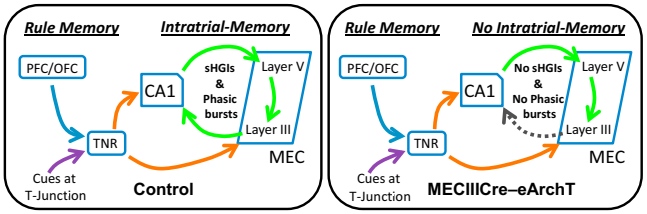

Figure 7. A Model of Neural Circuits Contributing to a Successful Execution of Spatial Working Memory and Its Failure by a Blockade of the MEC Input to dCA1

TNR, thalamic nucleus reuniens; PFC, prefrontal cortex; OFC, orbitofrontal cortex (see the text for more details). See also Figure S7.

Eichenbaum, 1992; Wallis et al., 2001) and can be routed by the thalamic nuclear reuniens (TNR) (Van der Werf et al., 2003; Vertes, 2004) to confer a valence to the T junction cues (Figure 7). In contrast, intratrial memory may be encoded in the known anatomical loop (van Strien et al., 2009) consisting of MECIII→CA1→MECV→MECIII (Figure 7). Several findings in our current study support this hypothesis. MECIII-TeTX mice (MT) and MECIII Cre-eArchT mice in which this loop is blocked or inhibited are impaired in the DNMP T maze task (Figures 1 and 6) (Suh et al., 2011). Moreover, these mice lack the ramping phasic bursts in MEC cells (Figures S5E and S5G) that are present in CTs while they run on the central track toward the T junction during success test trials, holding the intratrial working memory (Figures 3B, S5B and S5G). Because the site of the genetic blockade in MTs is at the MECIII→CA1 synapses rather than at the MECIII cell soma, the lack of ramping activity in the MEC of MTs is likely to be due to an impairment at the level of the neuronal circuit, for which the MEC-CA1-MEC loop is a good candidate. Furthermore, the finding that phasic bursts in CTs at the T junction are delayed in CA1 compared to MEC (Figures 5D and 5E) supports the role of this loop in holding the intratrial working memory.

Potential Mechanisms for MEC-CA1 High Gamma Synchronization

The direct MECIII-to-dCA1 pathway is also crucial for the generation of high gamma oscillations in CA1 (Figures 1C, 1D, and 2F). How could high gamma oscillations become synchronized between these two areas in a specific task context? One possibility is that the known bidirectional inhibition between them mediates synchrony (Melzer et al., 2012). Another possibility, which we favor (Figure 7 and the following discussion), is that the T-junction drives common inputs from the thalamic nucleus reunion (TNR), which is known to project directly to both the MEC and dCA1 (Dolleman-Van Der Weel and Witter, 1996; Vertes, 2004), and may act to coordinate corticohippocampal synchrony. Thus, the MEC→CA1 circuit is centrally positioned to integrate external perception and internal goal orientation—in this case, working memory association. Evidently, the animal's perception of local cues at the T junction may provide sensory evidence to the internal working memory loop, resulting in MEC-CA1 synchronization.

High Gamma Synchrony May Contribute to Explicit Awareness of Working Memory Content

Trained mice are expected to form intratrial working memory during the sample trials, but with the current set of data, we cannot pinpoint when they make the decision regarding the arm that they will choose subsequently. However, whenever the decision is made, this will become a part of the working memory for its execution at the T junction. The ramping MEC activity may represent increasing activity in the working memory-holding MEC→CA1→MEC loop. Such increasing activity may be driven by the accumulation of evidence as the animal approaches the T junction, including the build-up of internal anticipation. The known persistent activity in EC cells may also contribute to this activity build-up process (Figure S7) (Egorov et al., 2002). In the context of bound integration models (Kiani et al., 2008), the animal's goal orientation (e.g., the reward arm) may drive the perceptual matching of external T junction cues with the internal working memory association until the MEC→CA1→ MEC loop activity reaches a threshold for the correct arm choice; once this threshold is met, it may enable synchronization of high gamma incidents, which may contribute to making the animal explicitly aware of the working memory content for the correct action that is necessary to retrieve the reward. Thus, sHGIs may trigger a state transition from the hold phase to the use phase of the working memory associations. In accord, the absence of not only sHGIs, but also ramping MEC activity in the central arm, correlated with errors in arm choice (Figures 5C and S5D). In addition, the hypothesis that sHGIs contribute to explicit awareness of working memory content is supported by the association of sHGIs with the self-correction of errors during oops cases (Figures 4A, 4B, S3C, S4A, and S4C), as such behaviors are not easily explained by any known unconscious conditioned response. We speculate that similar high gamma synchrony operating in other brain areas may also index conscious control, including correction of mistakes as previously reported studies (Johnson and Redish, 2007; Resulaj et al., 2009).

(G) Effects of light restricted to the indicated periods and spatial locations in the T maze of the task performance on psHGI counts per trial during day 2 (light OFF) and day 3 (light ON) (*$p < 0.05$, paired t test; error bar represents SEM). See Experimental Procedures for the definition of psHGI.

(H) Relationship between psHGI in c1 and success rate of performance when illumination was targeted to the c1-c3 period of test trials (green), the c3-c5 period of test trials (orange), and the c1-c3 period of sample trials (blue). Each small dot represents an individual animal, whereas larger dots with error bars represent the average of each group (error bar represents SEM). psHGI occurred less frequently when light was delivered during c1-c3 in test trials compared to the other two conditions (*$p < 0.05$, **$p < 0.01$, one-tailed two-sample t test). Dotted lines indicate linear regression. Significant correlation was observed in light on condition (green) between psHGI and success rate (*$p < 0.05$).

(I) Theta-locked MUA was reduced during c1 and c2 when light was delivered during c1-c3 of test trials (*$p < 0.05$, **$p < 0.01$, paired t test; error bar represents SEM).

See also Figure S6.

EXPERIMENTAL PROCEDURES

Animals

All procedures relating to mouse care and treatment conformed to the institutional and NIH guidelines. Where mutant mice (MT or CT, see below) were not used, wild-type male C57BL/6 mice between 18 and 28 weeks of age were used. We previously developed a tetanus toxin (TeTX)-based triple-transgenic mouse (MECIII-TeTX MT) that allows for inducible and reversible silencing of synaptic transmission of MEC layer III pyramidal cells (Suh et al., 2011). As control mice, we used double-transgenic littermates of the triple-transgenic mice that lack the tTA transgene (MECIII-TeTX CT).

Delayed Nonmatch-to-Place T Maze Task

Delayed nonmatch-to-place (DNMP) T maze task was conducted with CT, MT, and wild-type male mice between 18 and 28 weeks of age. The task protocol used was similar to that previously reported (Suh et al., 2011), with minor modifications in intertrial interval and maze size, as shown in Figure 1E.

In Vivo Electrophysiology

Single shank silicone probes (HPC: A1x32-6mm-50-177-H32_21mm or A1x32-6mm-25-177-H32_21mm, MEC: A1x32-5mm-25-177-H32_21mm, NeuroNexus) were used. Each probe was mounted on a custom-designed miniature microdrive (3.5 g, unpublished) that can take up to two sets of 32 channel silicone probes. A total of 34 mice were implanted with this microdrive. Twenty-three mice were used for the single-site recordings in the hippocampus, and 11 mice received HPC and MEC dual-site recordings in the later stage of the study. The recorded coordinates were as follows: [HPC] AP: −1.80 mm, ML: +1.70 mm, DV: +2.20 mm (adjustable); [MEC] AP: −4.50 mm, ML: +3.50 mm, DV: +2.00 mm (at 10 degrees anterior-to-posterior). All recordings were conducted after the mice were fully recovered (at least 7 days after the surgery). Once all recording sessions were over, the animals were deeply anesthetized and postmortem histology was performed for a subsequent electrode track position reconstruction. The fixed brains were cut into 50 μm thick slices and were stained with DAPI. In all cases, the electrode track and tip location were identified with the help of DiI fluorescence on the silicon probes. We combined the histology information with electrophysiologically unique features (for example, sharp-wave-ripple bursts from CA1 cell layer and current source density distributions) to identify the position of current sinks and sources along the somatodendritic axis of CA1 (see example Figure S1A). We used the recording sites that showed the highest sink magnitude during high gamma oscillations, namely SLM area of CA1. MEC recording sites were identified with an approach similar to CA1, although we did not see a clear electrophysiological boundary between layer 2 and layer 3 of MEC, and data from both layers were combined.

Electrophysiology with Pharmacology Manipulation in MEC

Pharmacological manipulation was conducted as previously reported (Suh et al., 2011). A mixture of scopolamine hydrobromide (cholinergic muscarinic receptor 1 antagonist) and LY367385 (metabotropic glutamate receptor 1 antagonist) or vehicle was bilaterally injected into the MEC 30–60 min before electrophysiology recordings.

In-Vivo-Anesthetized Recordings

In-vivo-anesthetized recordings were conducted as previously described (Kitamura et al., 2014), with minor changes in the duration of light illumination and number of sweeps.

Virus Constructs

The AAVrh8-hSyn1-DIO-eArchT-eYFP plasmid was constructed by inserting the eArchT-eYFP gene fragment, which was obtained from a template, pLenti-CaMKIIa-eArchT_3.0eYFP (courtesy of Dr. Karl Deisseroth at Stanford University) (Mattis et al., 2012). This fragment was cloned into AscI (1165 bp) and NcoI sites (2719 bp) of a linearized and modified AAV vector containing the human synapsin1 promoter, using the double-floxed inverted construct strategy (Atasoy et al., 2008). Restriction digests were made according to standard protocol, and ligations were made using Takara DNA ligation kit version 2.1. The construct was amplified using EndoFree Plasmid QIAGEN maxi prep kit. Recombinant AAV vectors were serotyped with AAVrh8 coat proteins and were packaged by the viral vector core at the Gene Therapy center and Vector Core at the University of Massachusetts Medical School. The final viral concentration was 1×10^{13} genome copies ml^{-1}.

Stereotactic Injection and Hybrid Fiber Optic Silicone Linear Probe Implant

Each animal underwent bilateral craniotomies using a 1/4 size drill bit at –4.50 mm anterioposterior (AP), ± 3.50 mm mediolateral (ML) for MEC injections. The AAVrh8 virus was injected using a mineral oil-filled glass micropipette joined by a microelectrode holder to a 10 μl Hamilton microsyringe. All mice were injected bilaterally with 250 nl AAV virus at a rate of 100 nl min^{-1}. After recovery from viral injection, two optical fibers were implanted to the left hemisphere of dorsal CA1 and MEC (coordinates: [HPC] AP: −1.80 mm, ML: −1.70 mm, DV: +1.30 mm; [MEC] AP: −4.50 mm, ML: −3.50 mm, DV: +2.00 mm at 10 degrees anterior-to-posterior). For the right hemisphere, two hybrid silicon probe arrays with an optical fiber (200 μm core) that was attached to the back of the probe were lowered through two right hemisphere holes at the following coordinates: [HPC] AP: −1.80 mm, ML: +1.70 mm, DV: +1.30 mm; [MEC] AP: −4.50 mm, ML: +3.50 mm, DV: +2.00 mm at 10 degrees anterior-to-posterior. All mice were allowed to recover for 7 days before subsequent experiments. All fiber placements and viral injection sites were verified histologically. We only included mice in this study that had fluorophore expression limited to MEC and dorsal CA1 stratum lacunosum moleculare (SLM) area.

Behavior and Electrophysiology with Optogenetic Manipulation

A yellow-green laser (561 nm, 500 mW; DPSS) with a custom-designed 2.5 m long fiber optics patch cable (dual 200 μm core, NA = 0.22, Doric Lenses) was installed on the same area where the T maze was situated. A custom-designed mechanical shutter using a digital high-speed servo motor (S3155, Futaba) was integrated at the laser outlet where the patch cable was connected. The shutter servo motor and the DPSS driver were controlled by custom-designed hardware based on a ATmega2560 microcontroller (Mega2560 Rev.3, Arduino), which monitored the animal's position via infrared photo beam sensors (PSR-11L, Kodenshi). and determined the laser timing for optogenetic intervention. The output power of the DPSS laser was calibrated to 20 mW with the implanted optical fiber attached. All viral-injected mice were subjected to the previously described training protocol for DNMP T maze task (see "Delayed Nonmatch-to-Place T Maze Task" in Experimental Procedures).

Behavior Position Extraction

All behavior positions were extracted based on the position of light-emitting diodes (LEDs) that were mounted on the headstage (preamp, 35 mm spacing). The overhead color camera monitored the animal's behavior, and the recording system (Digital Lynx) tracked the LED position at 30 Hz. Once the head-tracking LED position crosses the border between c1 and r1 segments, we scored the animal's performance during the test trials. Velocity filters were applied (central arm: 2 cm/s and reward arm: 0.5 cm/s) to extract valid run segments from the electrophysiological data. A lower velocity filter setting was used on the reward arm to reliably capture the oops cases, which usually occurred below 2 cm/s.

Selection of Low/High Gamma Bands in Mice

We performed cross-frequency analysis (Tort et al., 2008, Colgin et al., 2009, Belluscio et al., 2012) to determine the passband filter settings. Theta oscillation was extracted by applying a 6–12 Hz finite impulse response (FIR) passband with zero-phase shift filter function in Matlab. The peak and trough of theta waveforms are set to 90° and 270° in this study. A time-varying power of wideband LFP (1–500 Hz) was estimated using Morlet's wavelets in 2 Hz frequency steps. The estimated average power of each frequency step is plotted as a function of waveform-based theta cycle phases. The mean wavelet power was smoothed with a Gaussian kernel ($\sigma = 10$ deg) and is shown as a color-coded plot (Figure 1B). From this analysis, we identified two distinct

gamma oscillations that are phase locked to a specific phase of baseband theta oscillation: low side centered around 40 Hz, spanning from 25 Hz to 50 Hz, and high side centered around 90 Hz, spanning from 65 Hz to 100 Hz. We set the passband settings for the low and high gamma band as follows: 35–55 Hz and 65–120 Hz. We did not include oscillations higher than 120 Hz for high gamma to exclude the possibility of spike-bled contamination. The slight elevation in wavelet power around 300 degrees that seemed to spread from higher frequency may suggest this contamination (Figure 1B).

Power Spectral Density Analysis

In order to effectively estimate the power spectral density (PSD) of relatively shorter data sets (an order of several seconds per trial in the DNMP task), we used a parametric method, the modified covariance method (MCM), using the autoregressive (AR) model (Percival and Walden, 1993):

$$P(f) = \frac{1}{F_S} \frac{p}{\left| 1 - \sum_{k=1}^{p} a_p(k) e^{-j2\pi kf/F_S} \right|^2}$$

in which $a_p(k)$ is AR parameter, and F_S is the sampling frequency.

To compute spatially segmented PSDs, we constructed a large array by concatenating each segment data for all trials but restricted to within animal, and then we computed PSDs to reliably estimate the spectral density. The power of theta, low gamma, and high gamma were obtained by integrating the PSD estimates for 6–12 Hz, 35–55 Hz, and 65–120 Hz, respectively, for individual animal, and were then treated as a discrete value to perform statistical comparisons for CT and MT data sets (Figures 1G, 2B, and 2C).

Current Source Density Analysis

Current source density (CSD) analysis was used to determine the loci of source-sink pairs in dorsal CA1 area (Figure S1A). CSD analysis provides a physiological index of the location, direction, and density of transmembrane current flow of the corresponding depths of the recorded region (Csicsvari et al., 2003; Freeman and Nicholson, 1975; Mitzdorf and Singer, 1978). The CSD magnitude is computed as a second spatial derivative of the LFP signal, which is based on the assumption of the ohmic conductive medium, constant extracellular conductivity, equidistant electrode contacts, and dominant current flow along the dendrite (z axis, one dimensional):

$$I = -\sigma_Z \partial^2 \Phi / \partial z^2$$

in which σ is the conductivity tensor and Φ is the field potential, respectively.

Gamma Incident Detection

To estimate the phase synchrony between dCA1 and MEC, we first identified periods in which gamma power (in high or low gamma frequency range) exceeded the 3 SD level of the baseline for each gamma band while the animal's running velocity is higher than the thresholds (see "Behavior Position Extraction"). We detected gamma power peaks that exceeded the threshold (i.e., 3 SD of the baseline level) and then searched a time window around the gamma peak until the power reached the cutoff (1 SD) level at both ends. We defined the extracted time window as high or low "gamma incidents." We used this adaptive algorithm to define a time window for a gamma incident to stably accommodate the whole time window in which the gamma power elevated. Note that a similar procedure was used in a previous study but with a fixed time window (Colgin et al., 2009). This procedure was performed for both CA1 and MEC gamma oscillations, respectively.

Phase Synchrony Analysis

For each detected gamma incident (see "Gamma Incident Detection"), phase synchrony between MEC and dCA1 was computed (we called it "sHGI candidate" in Figures 3G–3J and S3) based on methods that have been described previously (Lachaux et al., 1999; Rodriguez et al., 1999) but were modified in this study to take both phase and power into account (color-coded figures in Figures 3, 4, and 5). The phase and power (i.e., square of amplitude value) were calculated for each frequency as a function of time by computing the Hilbert transform (Matlab). The phase and amplitude, $\Phi(t, n)$ and $A(t, n)$, were extracted for all time points, t, for each detected gamma incident, n [1,…, N], and for each pair of recordings. The phase synchrony was estimated at each time point, t, and for each frequency, f, by taking the average value across the detected gamma incidents:

$$PhaseSynchrony_t = \left[\frac{1}{N} \sum_{n=1}^{N} \exp(j(\Phi_1(t,n)) - j(\Phi_2(t,n))) \right] \times A_1(t,n) A_2(t,n)$$

We color plotted the real part of this index, $A1(t)A2(t)cos(\Phi_1(t)\text{-}\Phi_2(t))$, in the figures in which a warm color represents a positive value (i.e., dCA1 and MEC are "in-phase" state), whereas a cool color represents a negative value (i.e., dCA1 and MEC are "out-phase" state).

In the optogenetics experiments (Figure 6), we calculated pure phase synchrony (see below) in which we excluded the contribution of power (Lachaux et al., 1999; Rodriguez et al., 1999) and identified pure synchronized high gamma incident (psHGI):

$$PurePhaseSynchrony_t = \left[\frac{1}{N} \sum_{n=1}^{N} \exp(j(\Phi_1(t,n)) - j(\Phi_2(t,n))) \right]$$

We estimated the pure phase synchrony for only those incidents that appeared with a power greater than 2 SD both in CA1 and MEC, as the phase value of a synchronized high gamma incidence with small powers in LFPs tends to be susceptible to noise and thus needs a threshold in regard to the power (Saalmann et al., 2007; Hirabayashi et al., 2010).

To test the significance of the phase synchrony (both sHGI and psHGI), we performed a bootstrap shuffling test by computing pseudo-phase synchrony values from randomized MEC-CA1 recording pairs constructed by randomly pairing (1,000 times) the CA1 high gamma windows with nonsimultaneously recorded gamma windows from MEC; the p value was computed by the Monte Carlo method. The significant sHGI and psHGI events were chosen only if the Monte Carlo p values were smaller than 0.05.

Multiunit Activity Periodicity Analysis

We recorded neuronal spiking activities with the silicon linear probes. The spacing of the recording sites, designed to maximally sample along the somatodendritic axes of CA1 and MEC (50 μm equidistant), limited the ability to isolate single units, and thus multiunit activities (MUA) were used to estimate spiking activities. The recorded position of each electrode contact was reconstructed from the LFP/CSD profile, such as the location of sharp waves and/or ripples in the CA1 cell layer, as well as from postmortem histological confirmation using Di-I fluorescent dye (Figures 6A and 6B). In the MEC, MUA was recorded only from the superficial layers (i.e., layers II and III) due to the steep angle of the electrode implant (Figure 6B). The periodicity index (discrete normalized autocorrelation coefficient) was estimated to quantify the magnitude of the periodic MUA bursts using an autocorrelation coefficient (Gray and Singer, 1989; Perkel et al., 1967):

$$R_{XX'}(m) = \frac{\sum_{n=0}^{N-1} x'(n) x'(n+m)}{\sqrt{\sum_{n=0}^{N-1} x'(n)^2} \sqrt{\sum_{n=0}^{N-1} x'(n+m)^2}}$$

in which x(n) is individual MUA burst events and $x'(n) = x(n) - (1/N)\sum_{n=0}^{N-1} x(n)$.

The index was computed for each section (c1-c5) in every trial, and then the individual indexes were treated as individual sample values for the subsequent statistical test (Figures 5C, 6I, S5F, and S5G).

SUPPLEMENTAL INFORMATION

Supplemental Information includes Extended Experimental Procedures, seven figures, and one movie and can be found with this article online at http://dx.doi.org/10.1016/j.cell.2014.04.009.

ACKNOWLEDGMENTS

We thank G. Das for the viral construction; C. Lovett, M. Serock, C. Ragion, N. Nayyar, and K. Kajikawa for help with the viral injections and histology; J. Young, C. MacDonald, M. Pignatelli, T. Kitamura, and C. Yokoyama for comments and discussions on the manuscript; and other members of the Tonegawa lab for their support. This work was supported by the RIKEN Brain Science Institute (to S.T.), the Picower Institute Innovation Fund (to S.T.), and the Human Frontier Science Program (HFSP) fellowship (to D.T.).

Received: February 5, 2014
Revised: March 20, 2014
Accepted: April 8, 2014
Published: April 24, 2014

REFERENCES

Atasoy, D., Aponte, Y., Su, H.H., and Sternson, S.M. (2008). A FLEX switch targets Channelrhodopsin-2 to multiple cell types for imaging and long-range circuit mapping. J. Neurosci. *28*, 7025–7030.

Belluscio, M.A., Mizuseki, K., Schmidt, R., Kempter, R., and Buzsáki, G. (2012). Cross-frequency phase-phase coupling between θ and γ oscillations in the hippocampus. J. Neurosci. *32*, 423–435.

Bragin, A., Jandó, G., Nádasdy, Z., Hetke, J., Wise, K., and Buzsáki, G. (1995). Gamma (40-100 Hz) oscillation in the hippocampus of the behaving rat. J. Neurosci. *15*, 47–60.

Carr, M.F., Karlsson, M.P., and Frank, L.M. (2012). Transient slow gamma synchrony underlies hippocampal memory replay. Neuron *75*, 700–713.

Chrobak, J.J., and Buzsáki, G. (1998). Gamma oscillations in the entorhinal cortex of the freely behaving rat. J. Neurosci. *18*, 388–398.

Colgin, L.L., Denninger, T., Fyhn, M., Hafting, T., Bonnevie, T., Jensen, O., Moser, M.B., and Moser, E.I. (2009). Frequency of gamma oscillations routes flow of information in the hippocampus. Nature *462*, 353–357.

Csicsvari, J., Jamieson, B., Wise, K.D., and Buzsáki, G. (2003). Mechanisms of gamma oscillations in the hippocampus of the behaving rat. Neuron *37*, 311–322.

Dolleman-Van Der Weel, M.J., and Witter, M.P. (1996). Projections from the nucleus reuniens thalami to the entorhinal cortex, hippocampal field CA1, and the subiculum in the rat arise from different populations of neurons. J. Comp. Neurol. *364*, 637–650.

Egorov, A.V., Hamam, B.N., Fransén, E., Hasselmo, M.E., and Alonso, A.A. (2002). Graded persistent activity in entorhinal cortex neurons. Nature *420*, 173–178.

Fell, J., Klaver, P., Lehnertz, K., Grunwald, T., Schaller, C., Elger, C.E., and Fernández, G. (2001). Human memory formation is accompanied by rhinal-hippocampal coupling and decoupling. Nat. Neurosci. *4*, 1259–1264.

Freeman, J.A., and Nicholson, C. (1975). Experimental optimization of current source-density technique for anuran cerebellum. J. Neurophysiol. *38*, 369–382.

Fries, P., Reynolds, J.H., Rorie, A.E., and Desimone, R. (2001). Modulation of oscillatory neuronal synchronization by selective visual attention. Science *291*, 1560–1563.

Fries, P., Nikolić, D., and Singer, W. (2007). The gamma cycle. Trends Neurosci. *30*, 309–316.

Gray, C.M., and Singer, W. (1989). Stimulus-specific neuronal oscillations in orientation columns of cat visual cortex. Proc. Natl. Acad. Sci. USA *86*, 1698–1702.

Gray, C.M., König, P., Engel, A.K., and Singer, W. (1989). Oscillatory responses in cat visual cortex exhibit inter-columnar synchronization which reflects global stimulus properties. Nature *338*, 334–337.

Hirabayashi, T., Takeuchi, D., Tamura, K., and Miyashita, Y. (2010). Triphasic dynamics of stimulus-dependent information flow between single neurons in macaque inferior temporal cortex. J. Neurosci. *30*, 10407–10421.

Hirabayashi, T., Takeuchi, D., Tamura, K., and Miyashita, Y. (2013). Functional microcircuit recruited during retrieval of object association memory in monkey perirhinal cortex. Neuron *77*, 192–203.

Johnson, A., and Redish, A.D. (2007). Neural ensembles in CA3 transiently encode paths forward of the animal at a decision point. J. Neurosci. *27*, 12176–12189.

Jutras, M.J., Fries, P., and Buffalo, E.A. (2009). Gamma-band synchronization in the macaque hippocampus and memory formation. J. Neurosci. *29*, 12521–12531.

Kiani, R., Hanks, T.D., and Shadlen, M.N. (2008). Bounded integration in parietal cortex underlies decisions even when viewing duration is dictated by the environment. J. Neurosci. *28*, 3017–3029.

Kitamura, T., Pignatelli, M., Suh, J., Kohara, K., Yoshiki, A., Abe, K., and Tonegawa, S. (2014). Island cells control temporal association memory. Science *343*, 896–901.

Lachaux, J.P., Rodriguez, E., Martinerie, J., and Varela, F.J. (1999). Measuring phase synchrony in brain signals. Hum. Brain Mapp. *8*, 194–208.

Lisman, J.E., and Idiart, M.A. (1995). Storage of 7 +/- 2 short-term memories in oscillatory subcycles. Science *267*, 1512–1515.

Mattis, J., Tye, K.M., Ferenczi, E.A., Ramakrishnan, C., O'Shea, D.J., Prakash, R., Gunaydin, L.A., Hyun, M., Fenno, L.E., Gradinaru, V., et al. (2012). Principles for applying optogenetic tools derived from direct comparative analysis of microbial opsins. Nat. Methods *9*, 159–172.

Melzer, S., Michael, M., Caputi, A., Eliava, M., Fuchs, E.C., Whittington, M.A., and Monyer, H. (2012). Long-range-projecting GABAergic neurons modulate inhibition in hippocampus and entorhinal cortex. Science *335*, 1506–1510.

Mitzdorf, U., and Singer, W. (1978). Prominent excitatory pathways in the cat visual cortex (A 17 and A 18): a current source density analysis of electrically evoked potentials. Exp. Brain Res. *33*, 371–394.

Montgomery, S.M., and Buzsáki, G. (2007). Gamma oscillations dynamically couple hippocampal CA3 and CA1 regions during memory task performance. Proc. Natl. Acad. Sci. USA *104*, 14495–14500.

Otto, T., and Eichenbaum, H. (1992). Complementary roles of the orbital prefrontal cortex and the perirhinal-entorhinal cortices in an odor-guided delayed-nonmatching-to-sample task. Behav. Neurosci. *106*, 762–775.

Percival, D.B., and Walden, A.T. (1993). Spectral Analysis for Physical Applications (New York: Cambridge Univ. Press).

Perkel, D.H., Gerstein, G.L., and Moore, G.P. (1967). Neuronal spike trains and stochastic point processes. I. The single spike train. Biophys. J. *7*, 391–418.

Quilichini, P., Sirota, A., and Buzsáki, G. (2010). Intrinsic circuit organization and theta-gamma oscillation dynamics in the entorhinal cortex of the rat. J. Neurosci. *30*, 11128–11142.

Resulaj, A., Kiani, R., Wolpert, D.M., and Shadlen, M.N. (2009). Changes of mind in decision-making. Nature *461*, 263–266.

Rodriguez, E., George, N., Lachaux, J.P., Martinerie, J., Renault, B., and Varela, F.J. (1999). Perception's shadow: long-distance synchronization of human brain activity. Nature *397*, 430–433.

Saalmann, Y.B., Pigarev, I.N., and Vidyasagar, T.R. (2007). Neural mechanisms of visual attention: how top-down feedback highlights relevant locations. Science *316*, 1612–1615.

Singer, W. (1993). Synchronization of cortical activity and its putative role in information processing and learning. Annu. Rev. Physiol. *55*, 349–374.

Suh, J., Rivest, A.J., Nakashiba, T., Tominaga, T., and Tonegawa, S. (2011). Entorhinal cortex layer III input to the hippocampus is crucial for temporal association memory. Science *334*, 1415–1420.

Tort, A.B., Kramer, M.A., Thorn, C., Gibson, D.J., Kubota, Y., Graybiel, A.M., and Kopell, N.J. (2008). Dynamic cross-frequency couplings of local field potential oscillations in rat striatum and hippocampus during performance of a T-maze task. Proc. Natl. Acad. Sci. USA *105*, 20517–20522.

Van der Werf, Y.D., Jolles, J., Witter, M.P., and Uylings, H.B. (2003). Contributions of thalamic nuclei to declarative memory functioning. Cortex *39*, 1047–1062.

van Strien, N.M., Cappaert, N.L., and Witter, M.P. (2009). The anatomy of memory: an interactive overview of the parahippocampal-hippocampal network. Nat. Rev. Neurosci. *10*, 272–282.

Vertes, R.P. (2004). Differential projections of the infralimbic and prelimbic cortex in the rat. Synapse *51*, 32–58.

Wallis, J.D., Anderson, K.C., and Miller, E.K. (2001). Single neurons in prefrontal cortex encode abstract rules. Nature *411*, 953–956.